

Transformation of a high-dimensional color space for material classification

HUAJIAN LIU,^{1,*} SANG-HEON LEE,¹ AND JAVAAN SINGH CHAHL^{1,2}

¹School of Engineering, University of South Australia, Mason Lakes, Adelaide, SA 5095, Australia

²Joint and Operations Analysis Division, Defence Science and Technology Organisation, Canberra, Australia

*Corresponding author: huajian.liu@mymail.unisa.edu.au

Received 27 October 2016; revised 13 February 2017; accepted 15 February 2017; posted 17 February 2017 (Doc. ID 279565); published 13 March 2017

Images in red–green–blue (RGB) color space need to be transformed to other color spaces for image processing or analysis. For example, the well-known hue-saturation-intensity (HSI) color space, which separates hue from saturation and intensity and is similar to the color perception of humans, can aid many computer vision applications. For high-dimensional images, such as multispectral or hyperspectral images, transformation images to a color space that can separate hue from saturation and intensity would be useful; however, the related works are limited. Some methods could interpret a set of high-dimensional images to hue, saturation, and intensity, but these methods need to reduce the dimension of original images to three images and then map them to the trichromatic color space of RGB. Generally, dimension reduction could cause loss or distortion of original data, and, therefore, the transformed color spaces could not be suitable for material classification in critical conditions. This paper describes a method that can transform high-dimensional images to a color space called hyper-hue-saturation-intensity (HHSI), which is analogous to HSI in high dimensions. The transformation does not need dimension reduction, and, therefore, it can preserve the original information. Experimental results indicate that the hyper-hue is independent of saturation and intensity and it is more suitable for material classification of proximal or remote sensing images captured in a natural environment where illumination usually cannot be controlled. © 2017 Optical Society of America

OCIS codes: (100.0100) Image processing; (150.0150) Machine vision; (280.0280) Remote sensing and sensors.

<https://doi.org/10.1364/JOSAA.34.000523>

1. INTRODUCTION

The red–green–blue (RGB) color space, or color cube, is a trichromatic color space that was designed for color image acquisition or displaying, while it has limitations for image processing or analysis because color and intensity information is mixed [1–4]. When doing image processing or analysis, it is usually necessary to separate color from intensity (or lightness or value) and saturation. The more general approach is to transform images in RGB color space to other color spaces such as hue-saturation-value (HSV) [5], hue-saturation-lightness (HSL) [6], generalized lightness-hue-saturation (GLHS) [7], hue-saturation-intensity (HSI) [8,9], or Lab, where L is for lightness and a and b are color components [10]. In these color spaces, hue, saturation, and intensity (or lightness or value) are separated, and these indices are more like the human sense of colors. In particular, hue has proven to be a useful index for material classification in natural environments [3,11–13]. Analogous to the RGB color space, a set of multispectral or hyperspectral images can be considered in a high-dimensional color space. For computer vision tasks, such as material classification, it would

be desirable to transform images captured under unreliable illumination to a space in which hue is independent of intensity and saturation, but related works are limited. Some methods have been developed to display hyperspectral images in standard monitors for human observation and classification, and these methods could be used to interpret a set of high-dimensional images to hue, saturation, and intensity (or lightness or value). However, these methods need to first reduce the dimension of original images to three images and then map the three images to the RGB color space. The RGB space can therefore be transformed to a desired color space using the normal color space transformation methods [14,15]. Alternatively, the dimension reduced images can be directly mapped to a preferred space such as HSV [15].

The simplest way to interpret hyperspectral images is to select three spectral bands and then input them to red, green, and blue channels for display and human observation [14,15]. In a monitor, observers can sense the hyperspectral images as hue, saturation, and intensity, and the red, green, and blue images can be transformed to a preferred color space for further

processing. However, there are many possibilities for choosing the bands, and there are no statistical theories that can determine which bands are better than others. The most often used methods are choosing three widely spaced bands or three specific bands that can highlight a particular spectral feature [15].

A more elegant approach is to transform high-dimensional images to three principal component (PC) images by means of principal components analysis (PCA) [15,16], and then the first three PC images can be mapped to red, green, and blue channels. However, usually, the displayed images are in pseudo colors that lack semantic significance [14,15]. In other words, the “hue” transformed from three PC images cannot represent the hue of the original data. Recently, some work has been conducted to solve this problem, and the displayed images are more semantically related to the scenes observed by humans. Buchsbaum and Gottschalk [17] demonstrated that the achromatic, red-green and blue-yellow color opponents sensed by humans correspond to the statistical non-covariant information derived from PCA of the spectral sensitivities of the three classes of photoreceptors in human eyes. Inspired by this result, Tyo and Konsolakis [15] considered the first component of PCA as the value in HSV color space and the angle between the second and third components as hue. In this model, the “hue” derived from the PC images can represent the hue of the high-dimensional images in a better manner. However, as pointed out by Jacobson and Gupta [14], the amount of variance in each of the PC images differs between different images and it would not optimally transfer the information. Although PCA provides a solution for transforming a set of high-dimensional images to “hue” in some specific tasks, generally speaking, the PCA-based methods have a number of disadvantages because of the inherent mechanisms of the PCA algorithms. Prasad and Bruce [18] pointed out the limitations of PCA for hyperspectral target recognition. They presented theoretical evidence of the ineffectiveness of PCA for feature extraction of hyperspectral data and it showed that class separation may deteriorate after a PCA transformation. They suggest that PCA should not be employed by researchers as a preprocessing to solve small-sample-size problems for automated target recognition. The study by Jacobson and Gupta [14] also showed that when processing hyperspectral images, targets that occur only with a few pixels in an image have little effect on the overall covariance matrix and will not contribute significantly to the second and third PCs. For this reason, PCA presentation strategies are better suited to depicting large-scale image features, not for identifying small or isolated targets, and it should not be expected to preserve edges for visualization. Other literature claims that a disadvantage of the PCA is that the covariance matrix is difficult to evaluate in an accurate manner, and the directions maximizing variance do not always maximize information [19,20]. A typical work that avoided using PCA was presented by Jacobson and Gupta [14]. In their study, the hyperspectral images were linearly transformed to red, green, and blue bands by using a set of predefined weights called spectrally weighted envelopes (SWEs). However, the proposed method still needs dimension reduction, and the ways to define the SWE could change the original information.

To transform high-dimensional images to hue, the existing methods need to reduce dimensions, but no matter how elegant

the transformations are, the dimension-reduced images cannot truly represent the original data. Methods based on PCA or weighted envelopes are more suitable for displaying, which assists better human observations for large-scale features. For automatic material classification, preservation of the original and detail information is critical, so the transformation of high-dimensional images to a color space without dimension reduction is necessary. Restrepo [21] developed a tetrachromatic color space called hue-colorfulness-luminance, which was transformed from four-dimensional multispectral images. He used topological methods to derive the values of hue, but this work did not provide a formula that can conveniently calculate the values of hue, and the transformation was limited in four dimensions only. Currently, the most often used spectral classifier is spectral angle mapper (SAM), which is able to determine the spectral similarity between the spectral signatures of two pixels [22,23]. If the angle between two spectral signatures is smaller than a predefined threshold, it indicates high similarity of the two pixels; similarly, a bigger angle indicates a low similarity. However, SAM measures only the relative angular distance between two spectral signatures, and the value of a spectral angle does not have a fixed meaning related to a material. For example, two types of materials with different spectral signatures could have the same spectral angle between a target signature and the two types of material cannot be classified by SAM.

This paper proposes a method that can transform high-dimensional images to a color space that is composed of hyper-hue, saturation, and intensity, and the transformed color space is called HHSI in this paper. For a set of n -dimensional images, the hyper-hue is represented by $(n - 1)$ -dimensional vectors, while saturation and intensity are similar to those in HSI color space as proposed by Hanbury [24]. Because hyper-hue does not introduce the loss or distortion of information from dimensional reduction and it is independent of saturation and intensity, it can be used as an index for material classification in natural environments where illumination is unstable. Section 2.B starts the derivation of a four-dimensional hyperchromatic space projected from a five-dimensional color hypercube and then generalizes the derivation to n -dimensions. Based on that, it provides the formulas to calculate the values of hyper-hue, saturation, and intensity. Section 3 describes three experiments, and then Section 4 draws the conclusions.

2. TRANSFORMATION OF COLOR HYPERCUBE TO HYPERCHROMATIC SPACE

A. Introduction of Color Hypercube and Hyperchromatic Space

In a RGB cube, the corner $(0, 0, 0)$ is “black” and $(1, 1, 1)$ is “white.” The segment that connects $(0, 0, 0)$ and $(1, 1, 1)$ is called the achromatic axis. When all the points in the RGB cube are projected to a plane that is perpendicular to the achromatic axis and includes the point $(0, 0, 0)$, the projection is called chromatic plane whose border is a regular hexagon. This concept can be expanded to a high-dimensional color hypercube. Suppose there is a five-dimensional color hypercube that includes five components x_1, x_2, x_3, x_4 , and x_5 . The hypercube is a space I^5 , where $I \in [0, 1]$. In this hypercube, the corner

$(0, 0, 0, 0, 0)$ is “black” and $(1, 1, 1, 1, 1)$ is “white.” By connecting the two corners, it has a segment that has the property of $x_1 = x_2 = x_3 = x_4 = x_5$ and the corresponding vector $\mathbf{a} = [1 \ 1 \ 1 \ 1 \ 1]^T$ is called hyperachromatic axis. A space I^4 perpendicular to the hyperachromatic axis and including the point $(0, 0, 0, 0, 0)$ is selected. All the points in the hypercube are projected to this space, and the projection will be called hyperchromatic space.

B. Derivation of a Hyperchromatic Space from a Five-Dimensional Hypercube

First, to derive the hyperchromatic space, four orthonormal vectors $\mathbf{u}_1, \mathbf{u}_2, \mathbf{u}_3$, and \mathbf{u}_4 , which span the hyperchromatic space, are defined. The four unit vectors have the following properties: (1) they have the origin $(0, 0, 0, 0, 0)$; (2) they are orthogonal to each other; (3) the norm of each vector is 1; (4) \mathbf{u}_1 points to the projection of the point $(1, 0, 0, 0, 0)$ in the hyperchromatic space; and (5) they are orthogonal to the hyperachromatic axis \mathbf{a} . Any vector projected to the hyperchromatic space can be expressed as a linear combination of the four unit vectors; hence, the derivation of the hyperchromatic space is to derive the four unit vectors. Figure 1 shows parts of the five-dimensional color hypercube. Because the figure is a two-dimensional projection of the five-dimensional hypercube, it has limitations in presenting the hypercube; hence, it shows only the first three components, x_1, x_2 and x_3 , and the first two unit vectors \mathbf{u}_1 and \mathbf{u}_2 . Let $\mathbf{u}_1 = [u_{11} \ u_{12} \ u_{13} \ u_{14} \ u_{15}]^T$ and \mathbf{p}_1 be a point on the axis of x_1 . From the properties of \mathbf{u}_1 , \mathbf{u}_1 is in the space spanned by \mathbf{a} and \mathbf{p}_1 , and that is $\mathbf{u}_1 = m\mathbf{a} + n\mathbf{p}_1$, where m and n are real numbers. Alternatively, this formula can be expressed as

$$\begin{bmatrix} u_{11} & u_{12} & u_{13} & u_{14} & u_{15} \end{bmatrix} = m[1 \ 1 \ 1 \ 1 \ 1] + n[x_1 \ 0 \ 0 \ 0 \ 0]. \quad (1)$$

From Eq. (1), we have

$$u_{12} = u_{13} = u_{14} = u_{15}. \quad (2)$$

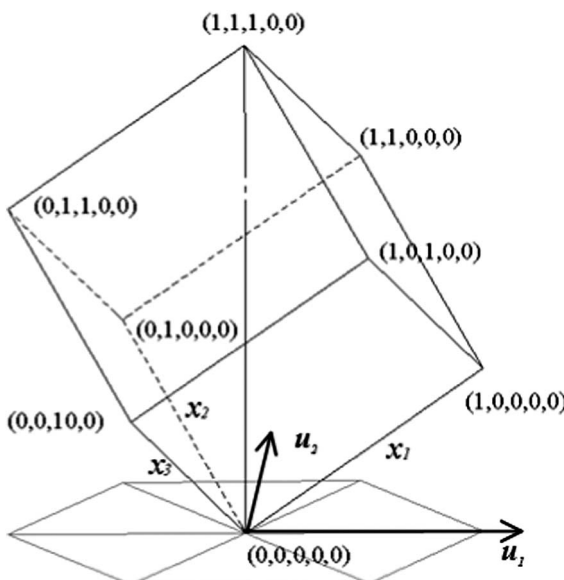


Fig. 1. Two-dimensional projection of a five-dimensional color hypercube.

Because \mathbf{u}_1 is orthogonal to \mathbf{a} , $\mathbf{u}_1 \cdot \mathbf{a} = 0$, and that is

$$u_{11} + u_{12} + u_{13} + u_{14} + u_{15} = 0. \quad (3)$$

With the constraint that \mathbf{u}_1 is a unit vector, we have

$$u_{11}^2 + u_{12}^2 + u_{13}^2 + u_{14}^2 + u_{15}^2 = 1. \quad (4)$$

From Eqs. (2)–(4), \mathbf{u}_1 can be solved:

$$\mathbf{u}_1 = \left[\frac{2}{\sqrt{5}} \ -\frac{1}{2\sqrt{5}} \ -\frac{1}{2\sqrt{5}} \ -\frac{1}{2\sqrt{5}} \ -\frac{1}{2\sqrt{5}} \right]^T. \quad (5)$$

Suppose there is another point $\mathbf{p}_2 = [x_1 \ x_2 \ 0 \ 0 \ 0]^T$, and \mathbf{u}_2 must be in the space spanned by \mathbf{a} and \mathbf{p}_2 , which is $\mathbf{u}_2 = m\mathbf{a} + n\mathbf{p}_2$. Similar to Eq. (1), it can be proven that

$$u_{23} = u_{24} = u_{25}. \quad (6)$$

Because \mathbf{u}_2 is perpendicular to \mathbf{a} and \mathbf{u}_1 , it is perpendicular to the axis x_1 and, therefore, $u_{21} = 0$. From $\mathbf{u}_2 \cdot \mathbf{a} = 0$ and that \mathbf{u}_2 is a unit vector, we have

$$u_{22} + u_{23} + u_{24} + u_{25} = 0, \quad (7)$$

$$u_{22}^2 + u_{23}^2 + u_{24}^2 + u_{25}^2 = 1. \quad (8)$$

From Eqs. (7) and (8), \mathbf{u}_2 can be solved:

$$\mathbf{u}_2 = \left[0 \ \frac{\sqrt{3}}{2} \ -\frac{\sqrt{3}}{6} \ -\frac{\sqrt{3}}{6} \ -\frac{\sqrt{3}}{6} \right]^T. \quad (9)$$

Suppose there exists a point $\mathbf{p}_3 = [x_1 \ x_2 \ x_3 \ 0 \ 0]^T$. Similarly, \mathbf{u}_3 must be in the space spanned by \mathbf{a} and \mathbf{p}_3 , and that is $\mathbf{u}_3 = m\mathbf{a} + n\mathbf{p}_3$. The same as in Eqs. (1) and (6), we have

$$u_{34} = u_{35}. \quad (10)$$

The space spanned by \mathbf{a}, \mathbf{u}_1 , and \mathbf{u}_2 is

$$m\mathbf{a} + n\mathbf{u}_1 + q\mathbf{u}_2 = \left[\begin{array}{ccccc} 1 & 1 & 1 & 1 & 1 \\ \frac{2}{\sqrt{5}} & -\frac{1}{2\sqrt{5}} & -\frac{1}{2\sqrt{5}} & -\frac{1}{2\sqrt{5}} & -\frac{1}{2\sqrt{5}} \\ 0 & \frac{\sqrt{3}}{2} & -\frac{\sqrt{3}}{6} & -\frac{\sqrt{3}}{6} & -\frac{\sqrt{3}}{6} \end{array} \right]^T \begin{bmatrix} m \\ n \\ q \end{bmatrix}, \quad (11)$$

where m, n , and q are real numbers. When

$$[m \ n \ q] = [1/5 \ 2/\sqrt{5} \ 0],$$

\mathbf{a}, \mathbf{u}_1 , and \mathbf{u}_2 span $[1 \ 0 \ 0 \ 0 \ 0]^T$, which is on the axis x_1 , and when

$$[m \ n \ q] = [1/5 \ -2/\sqrt{5} \ \sqrt{3}/2],$$

they span $[0 \ 1 \ 0 \ 0 \ 0]^T$, which is on the axis x_2 . Therefore, the axes x_1 and x_2 are in the space spanned by \mathbf{a}, \mathbf{u}_1 , and \mathbf{u}_2 . Because \mathbf{u}_3 is perpendicular to the space spanned by \mathbf{a}, \mathbf{u}_1 , and \mathbf{u}_2 , \mathbf{u}_3 is perpendicular to the axis x_1 and x_2 ; hence, $u_{31} = u_{32} = 0$. Also, $\mathbf{u}_3 \cdot \mathbf{a} = 0$ and \mathbf{u}_3 is a unit vector, so we have

$$u_{33} + u_{34} + u_{35} = 0, \quad (12)$$

$$u_{33}^2 + u_{34}^2 + u_{35}^2 = 1. \quad (13)$$

From Eqs. (12) and (13), \mathbf{u}_3 can be solved:

$$\mathbf{u}_3 = \left[0 \ 0 \ \sqrt{\frac{2}{3}} \ -\sqrt{\frac{1}{6}} \ -\sqrt{\frac{1}{6}} \right]^T. \quad (14)$$

Because \mathbf{u}_4 is orthogonal to \mathbf{a} , \mathbf{u}_1 , \mathbf{u}_2 , and \mathbf{u}_3 , that same as \mathbf{u}_3 , it can be proven that $u_{41} = u_{42} = u_{43} = 0$. Also, as $\mathbf{u}_4 \cdot \mathbf{a} = 0$ and \mathbf{u}_4 is a unit vector, we have

$$u_{44} + u_{45} = 0, \quad (15)$$

$$u_{44}^2 + u_{45}^2 = 1. \quad (16)$$

From Eqs. (15) and (16), \mathbf{u}_4 can be solved:

$$\mathbf{u}_4 = \begin{bmatrix} 0 & 0 & 0 & \sqrt{\frac{1}{2}} & -\sqrt{\frac{1}{2}} \end{bmatrix}^T. \quad (17)$$

If the projection of a point \mathbf{x} in the hypercube to the hyperchromatic space is \mathbf{c} and its four components in the direction of \mathbf{u}_1 , \mathbf{u}_2 , \mathbf{u}_3 , and \mathbf{u}_4 are \mathbf{c}_1 , \mathbf{c}_2 , \mathbf{c}_3 , and \mathbf{c}_4 , \mathbf{c} can be solved by

$$\mathbf{c}_1 = (\mathbf{x} \cdot \mathbf{u}_1)\mathbf{u}_1$$

$$= \left(\frac{2}{\sqrt{5}}x_1 - \frac{1}{2\sqrt{5}}x_2 - \frac{1}{2\sqrt{5}}x_3 - \frac{1}{2\sqrt{5}}x_4 - \frac{1}{2\sqrt{5}}x_5 \right) \mathbf{u}_1, \quad (18)$$

$$\mathbf{c}_2 = (\mathbf{x} \cdot \mathbf{u}_2)\mathbf{u}_2 = \left(\frac{\sqrt{3}}{2}x_2 - \frac{\sqrt{3}}{6}x_3 - \frac{\sqrt{3}}{6}x_4 - \frac{\sqrt{3}}{6}x_5 \right) \mathbf{u}_2, \quad (19)$$

$$\mathbf{c}_3 = (\mathbf{x} \cdot \mathbf{u}_3)\mathbf{u}_3 = \left(\sqrt{\frac{2}{3}}x_3 - \sqrt{\frac{1}{6}}x_4 - \sqrt{\frac{1}{6}}x_5 \right) \mathbf{u}_3, \quad (20)$$

$$\mathbf{c}_4 = (\mathbf{x} \cdot \mathbf{u}_4)\mathbf{u}_4 = \left(\sqrt{\frac{1}{2}}x_4 - \sqrt{\frac{1}{2}}x_5 \right) \mathbf{u}_4, \quad (21)$$

$$\mathbf{c} = \mathbf{c}_1 + \mathbf{c}_2 + \mathbf{c}_3 + \mathbf{c}_4. \quad (22)$$

C. Derivation of a Hyperchromatic Space from an N -Dimensional Hypercube

By the observation of Eqs. (5), (9), (14), and (17), \mathbf{u}_1 does not have zero elements; \mathbf{u}_2 has one zero element u_{21} ; \mathbf{u}_3 has two zero elements u_{31} and u_{32} , and so on. In addition to that, for each of the unit vectors \mathbf{u}_1 to \mathbf{u}_5 , except the zero elements and the first non-zero element, other elements are all equal. In other words, for any vector of \mathbf{u}_1 to \mathbf{u}_5 , the number of unknown elements is two. With the two constraints that the norms of \mathbf{u}_1 to \mathbf{u}_5 are all equal to 1 and they are orthogonal to \mathbf{a} , \mathbf{u}_1 to \mathbf{u}_5 can be solved. Suppose there is an n -dimensional hypercube projected to a hyperchromatic space that is spanned by the unit vectors of \mathbf{u}_1 , \mathbf{u}_2 , ..., \mathbf{u}_{n-1} , where n is a natural number equal to or more than 2. If one of the unit vectors \mathbf{u}_i has the form of $\mathbf{u}_i = [u_{i1} \ u_{i2} \ \dots \ u_{in}]^T$, then from Eqs. (23)–(26) \mathbf{u}_i can be solved; hence, the hyperchromatic space in $(n-1)$ dimensions is derived:

$$u_{i1} = u_{i2} = \dots = u_{i(i-1)} = 0, \quad (23)$$

$$u_{i(i+1)} = u_{i(i+2)} = \dots = u_{in}, \quad (24)$$

$$u_{i1}^2 + u_{i2}^2 + \dots + u_{in}^2 = 1, \quad (25)$$

$$u_{i1} + u_{i2} + \dots + u_{in} = 0. \quad (26)$$

Suppose a unit vector \mathbf{u}_i has m non-zero elements, and the first one is equal to a and others are equal to b , a and b can be solved as

$$a = \sqrt{m-1}/\sqrt{m}, \quad (27)$$

$$b = -1/\sqrt{m-1}\sqrt{m}. \quad (28)$$

D. Discussion of Hyperchromatic Space and Derivation of Hyper-Hue, Saturation, and Intensity

A chromatic plane projected from a RGB color cube is a regular hexagon. Similarly, the hyperchromatic space projected from a color hypercube includes two or more hexagons that are perpendicular to each other. The border of the hyperchromatic space is composed of many triangles that are formed by connecting the corners of these hexagons. To visualize a three-dimensional hyperchromatic space, one can create a four-dimensional hypercube and then project it to a hyperchromatic space. Suppose the four components of a color hypercube URGB are U , R , G , and B , where U represents a certain spectral band and R , G , and B represent red, green, and blue, respectively. Twenty-one sampling points are evenly distributed in each dimension of U , R , G , and B in the domain of $[0,1]$. The projection of a point from the four-dimensional hypercube to a three-dimensional hyperchromatic space is \mathbf{c} , which has three components \mathbf{c}_1 , \mathbf{c}_2 , and \mathbf{c}_3 . The three-dimensional shape of the hyperchromatic space is not obvious when it is projected to a two-dimensional figure, but the profiles of it from certain directions are clear. Figure 2 shows the profile of \mathbf{c}_2 and \mathbf{c}_3 when \mathbf{c}_1 is zero. Figure 3 shows the profile of \mathbf{c}_1 and \mathbf{c}_3 when \mathbf{c}_2 is zero. Figure 4 shows the profile of \mathbf{c}_1 and \mathbf{c}_2 when \mathbf{c}_3 is zero. \mathbf{c}_2 and \mathbf{c}_3 are calculated from R , G , and B and do not include the information of U . As in Fig. 2, the profile of \mathbf{c}_2 and \mathbf{c}_3 is a regular hexagon, which is same as the chromatic plane projected from a RGB cube. The points in the profile of \mathbf{c}_2 and \mathbf{c}_3 have defined colors that are composed of R , G , and B , and, therefore, the profile was marked with the corresponding colors. \mathbf{c}_1 is calculated from U , R , G , and B and as shown in Figs. 3 and 4, the profile composed of \mathbf{c}_1 and \mathbf{c}_3 or \mathbf{c}_1 and \mathbf{c}_2 is a non-regular hexagon. Because the points in the profile of \mathbf{c}_1 and \mathbf{c}_3 or \mathbf{c}_1 and \mathbf{c}_2 are in some undefined colors, they are marked as gray.

For a point \mathbf{c} in a hyperchromatic space, the direction of it is hyper-hue. Different from the normal hue, the hyper-hue is not

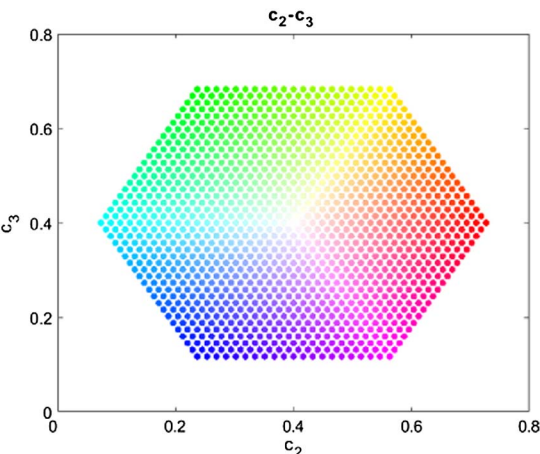


Fig. 2. Profile of \mathbf{c}_2 and \mathbf{c}_3 when \mathbf{c}_1 is zero.

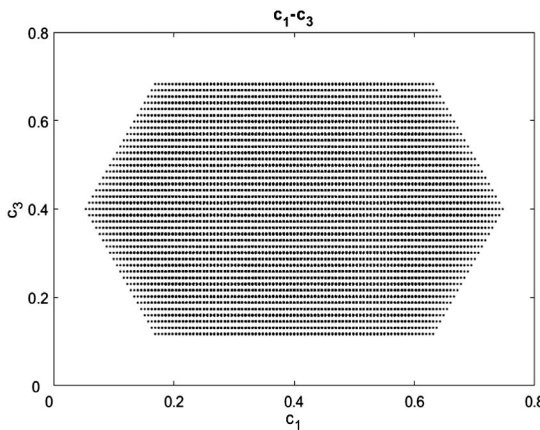


Fig. 3. Profile of \mathbf{c}_1 and \mathbf{c}_3 when \mathbf{c}_2 is zero.

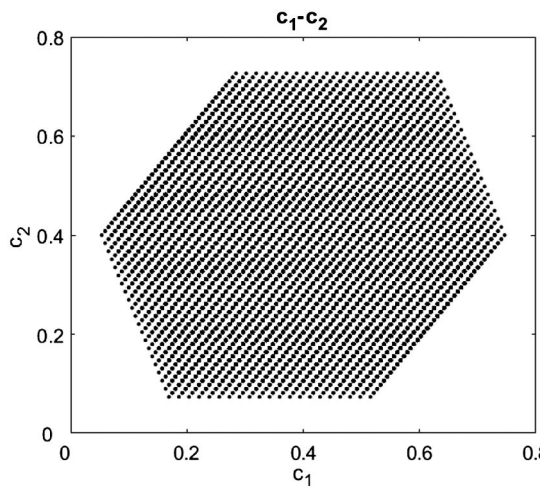


Fig. 4. Profile of \mathbf{c}_1 and \mathbf{c}_2 when \mathbf{c}_3 is zero.

in one dimension and it cannot be presented at an angle from 0° to 360° . The simplest expression of hyper-hue \mathbf{h} is given by Eq. (29), where $\|\mathbf{c}\|$ is the norm of \mathbf{c} :

$$\mathbf{h} = \frac{\mathbf{c}}{\|\mathbf{c}\|}. \quad (29)$$

For an n -dimensional color hypercube, the \mathbf{h} is in $(n-1)$ dimensions and the norm of it is always equal to 1; hence, it can represent the direction of \mathbf{c} . Note that if x_3 , x_4 , and x_5 are replaced by R , G , and B , respectively, in Eqs. (20) and (21), the angle h between \mathbf{c}_3 and \mathbf{c}_4 is

$$h = \arctan\left(\frac{\sqrt{3}(G-B)}{2R-G-B}\right). \quad (30)$$

Equation (30) is the expression of hue by Hanbury [24]. When changing the arctan form into arccos form, it is the formula of hue by Gonzalez and Woods [8]. This observation indicates that if the last three components of a hypercube are red, green, and blue, then the chromatic plane projected from a RGB cube is a subspace of the hyperchromatic space, and the

hue defined in a two-dimensional chromatic plane is a subspace of the hyper-hue.

While the definitions of hue are similar in the color space of HSV, HSL, and HSI, the definitions of saturation are different. One of the widely accepted definitions of saturation has the form of $\max\{R, G, B\} - \min\{R, G, B\}$. Hanbury [24] proved that $\max\{R, G, B\} - \min\{R, G, B\}$ is the normalized form of chroma. In his model, as shown in Fig. 5, for a vector \mathbf{c} in a two-dimensional chromatic plane, the definition of chroma c is the norm of \mathbf{c} and that is $c = \|\mathbf{c}\|$. When extending \mathbf{c} to the border of the chromatic plane to have a vector \mathbf{c}_{max} , saturation s is the normalized value of $\|\mathbf{c}\|$ as in

$$s = \frac{\|\mathbf{c}\|}{\|\mathbf{c}_{max}\|} = \max\{R, G, B\} - \min\{R, G, B\}. \quad (31)$$

This definition of saturation is reasonable and has the most concise form. In a chromatic plane, if the values of chroma c are replaced by that of saturation s , then the border of the chromatic plane transforms from a hexagon to a circle. This definition of saturation can be expanded to a hyperchromatic space and it has the form of

$$s = \frac{\|\mathbf{c}\|}{\|\mathbf{c}_{max}\|} = \max\{x_1, x_2, \dots, x_n\} - \min\{x_1, x_2, \dots, x_n\}, \quad (32)$$

where x_1, x_2, \dots, x_n are the color components of a hypercube and n is a natural number more than 2. When replacing the values of chroma by the values of saturation in a three-dimensional hyperchromatic space, the border of it expands to a sphere and the space enclosed within it is the normalized hyperchromatic space. Figure 6 shows three profiles of a three-dimensional normalized hyperchromatic space projected from a hypercube URGBC. In Fig. 6, the points projected from the RGB cube were marked with the corresponding colors, while other points are marked with gray or black since there are no corresponding color definitions for these points.

The definition of intensity i can be simply expressed as

$$i = \frac{1}{n}(x_1 + x_2 + \dots + x_n), \quad (33)$$

which is analogous to the intensity in the HSI space proposed by Hanbury [24]. However, there are no constraints to define the analogous value in HSV [5] or lightness in HSL [6].

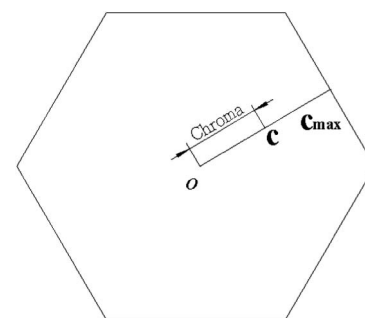


Fig. 5. Definition of chroma by Hanbury [24].

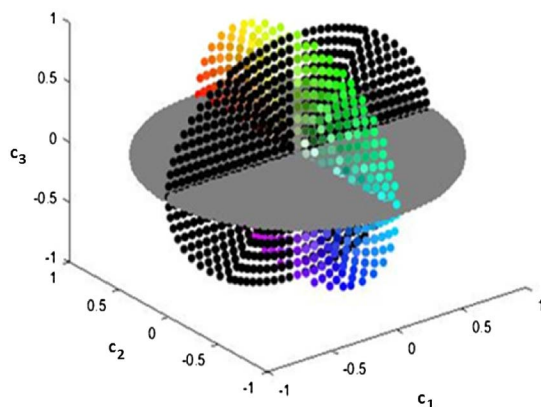


Fig. 6. Profiles of a three-dimensional normalized hyperchromatic space.

3. EXPERIMENTS

A. Experiment One: Material Classification Under Uneven Illumination

This experiment aimed to assess the power of hyper-hue for material classification under uneven illumination. A green leaf, pieces of green paper and blue paper were laid on an orange background for imaging. The purpose was to classify the four types of materials using the captured image. As shown in Fig. 7(a), because the colors of the leaf and the green paper are very close, using the color image only would lack the robustness of classification. Near-infrared (NIR) has proven to be useful to distinguish green plants from other materials [12], so this experiment used the combination of NIR, red, green, and blue

images for classification. An AD-130GE (JAI, Yokohama, Japan) machine vision camera was used to capture the multispectral images. The camera is capable of simultaneously capturing both color images and NIR images through the same optical lens (1214, Pentax, Tokyo, Japan) using two different CCD sensors, and the captured images are pairwise registered. The lights were intentionally arranged so that the illumination in the field of view (FOV) of the camera was uneven. As shown in Figs. 7(a) and 7(b), the top right corner is darker than other areas. There are many mathematical classifiers available for data classification, and one of the most generally used unsupervised machine learning algorithms k-means++ [25] was used for classification in this experiment.

Two methods were compared for classification. The first method directly input the captured images of NIR, red, green, and blue to the k-means++ algorithm. As expected, this method cannot obtain correct classification because the values of these images are mixtures of color and intensity. As shown in Fig. 7(c), the uneven illumination misled the classification algorithm. The second method first transformed the multispectral images to hyper-hue and then used it for classification. Figures 7(d)–7(f) show the images of hyper-hue in three dimensions and Fig. 7(g) show the classification result. Compared with the first method, using hyper-hue can achieve a relatively satisfied result. As shown in Fig. 7(g), it correctly classified the materials into four groups in which the background, blue paper, green paper, and leaf are presented as black, white, dark gray, and light gray, respectively. There are a few noises near the borders of the objects, but these noises are acceptable and can be removed using general image processing methods. This experiment indicated that the hyper-hue is invariant to the change of illumination, and that it would

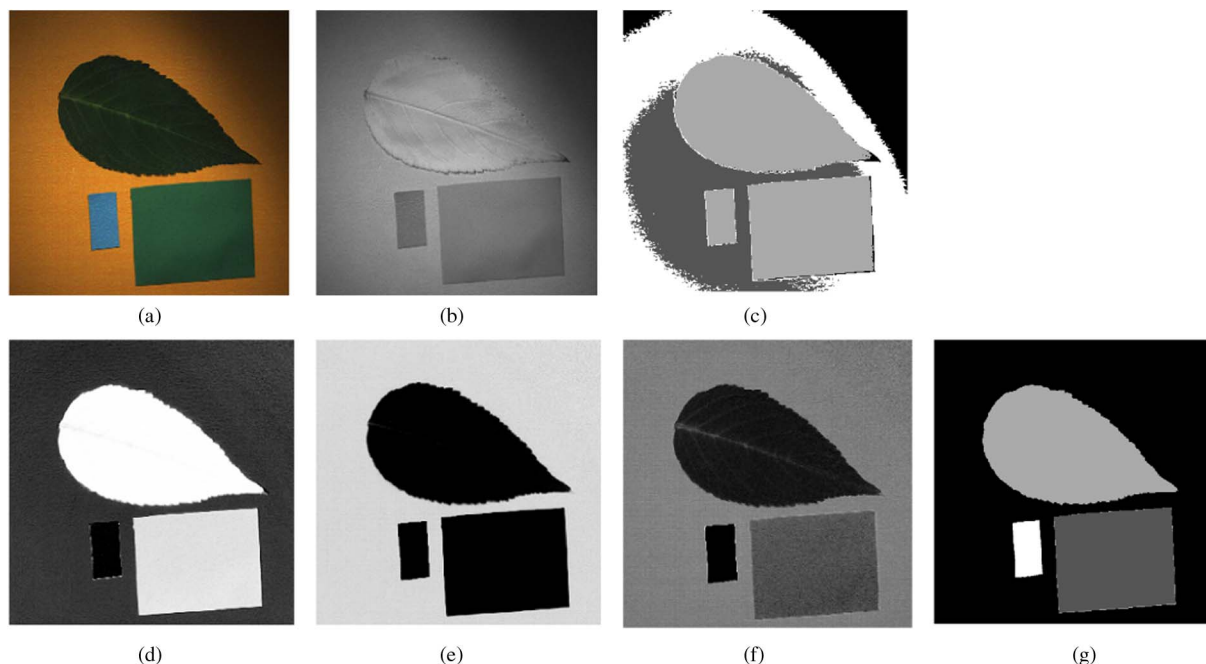


Fig. 7. K-means++ classification using the original data and hyper-hue. (a) The original color image, (b) the original NIR image, (c) the classification result using the original data, (d) the image of the first dimension of hyper-hue, (e) the image of the second dimension of hyper-hue, (f) the image of the third dimension of hyper-hue, and (g) the classification result using hyper-hue.

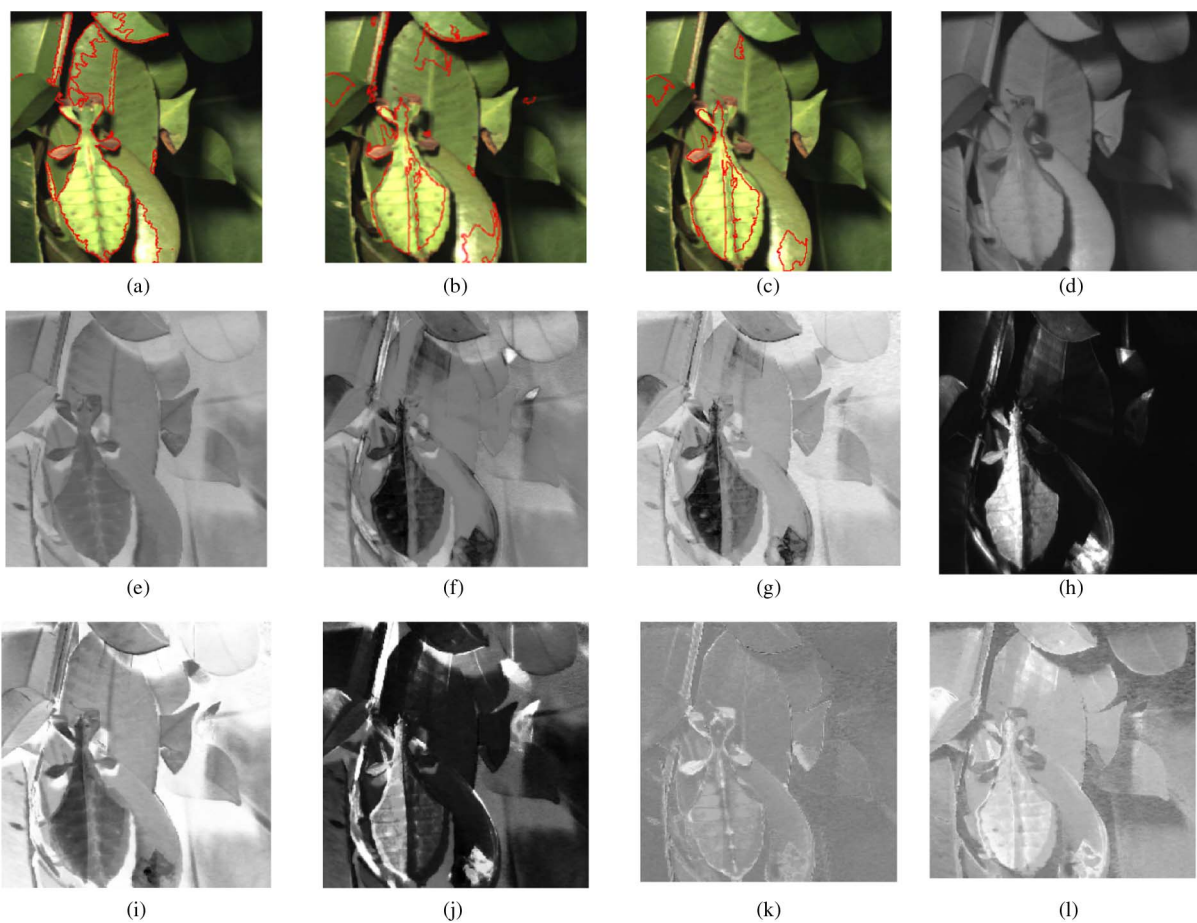


Fig. 8. Example images for the classification of leaf insects and leaves. (a) Classification result using NDVI, (b) classification result using SAM, (c) classification result using hyper-hue, (d) original image of NIR, (e) image of normalized NDVI(N_n), (f) image of normalized SAM (N_s), (g) image of normalized distance of hyper-hue (N_h), (h) original image of UV, (i) the first dimension of hyper-hue, (j) the second dimension of hyper-hue, (k) the third dimension of hyper-hue, and (l) the fourth dimension of hyper-hue.

be suitable for material classification tasks when lighting conditions are not ideal. Note that there are other methods that could overcome the challenge of uneven illumination, while hyper-hue provides an additional approach that would be more convenient for some specific tasks.

B. Experiment Two: Classification of Insects from Green Leaves

Detecting insect pests on crops is a strategy for modern integrated pest management and precision agriculture [11,26]. However, it is extremely challenging for a machine vision system (MVS) to detect insect pests in their living environments, where there are usually uneven illumination and complex background, especially for some camouflaged insects that have the same color, textural, and morphological features as the environment they live in. An experiment was conducted to classify leaf insects (family: Phyllidae) from leaves of bushes (family: Caprifoliaceae) in ultraviolet (UV), blue, green, red, and NIR multispectral images. A leaf insect was selected as a specimen because it is one of the most remarkably camouflaged animals, and if an MVS can detect this type of insect on plants then the most common pests can be detected.

The hardware of the MVS included a machine vision camera with lens, filter set, and a computer. The monochrome camera (CM-140GE-UV, JAI, Yokohama, Japan) has a broadband response from UV at 200 nm to NIR at 780 nm. The lens (GMUV42528C, Goyo, Saitama, Japan) allows light from 200 to 1200 nm to pass through. Five bandpass filters of UV, blue, green, red, and NIR were selected, and the peak wavelength and the full width at half-maximum (FWHM) of the filters are listed in Table 1. The filters were mounted on a filter rotating wheel allowing rapid exchanging of filters. When doing image acquisition, the leaf insects on the host plants were positioned

Table 1. Specification of the Filters of the MVS

Band	Peak (nm)	FWHM (nm)	Manufacturer
UV	330	85	U-340, HOYO, Tokyo, Japan
Blue	465	85	BP470, Midopt, Palatine, Illinois
Green	528	80	BP525, Midopt
Red	630	60	BP635, Midopt
NIR	748	90	BP735, Midopt

300–500 mm in front of the camera, and the images were captured under natural sunlight in cloudy weather. A total of 150 sets of multispectral images were captured and then saved on the computer for processing. Figures 8(a), 8(d), and 8(h) provide examples of the captured images.

Three methods were tested to classify the insects from the leaves. The first method used the normalized difference vegetation index (NDVI) [27]. NDVI remains the most well-known and used index to detect live green plant canopies in multispectral remote or proximal sensing data [3]. NDVI has the form of

$$\text{NDVI} = (IR - R)/(IR + R), \quad (34)$$

where IR represents the intensity values of NIR and R for red. The values are in the domain $[-1, 1]$, and a value near 1 means a high amount of chlorophyll, indicating green leaves [27]. To obtain proper values of NDVI, images captured from satellites or aircraft need radiometric calibration to compensate for the effects of atmosphere, clouds, and soil. In this study, the images were captured in close ranges and the effects of the environment can be ignored. Hence, the radiometric calibration was bypassed. The values of NDVI were further normalized to $[0,1]$ using

$$N_n = (\text{NDVI} + 1)/2, \quad (35)$$

where N_n is the normalized value of NDVI. As shown in Fig. 8(e), in the image of N_n , the intensity values of the insect are lower and those of the leaves are relatively higher. A threshold $t_n = 0.45$ was applied to classify the pixels as leaves or insects. The threshold t_n was obtained from the learning of a set of training data. Fifty sets of multispectral images were randomly selected from the captured images as training data, and then the images were processed using the algorithm described above. Each set of images was manually classified to provide a ground truth reference for correct classification. The manually processed images were compared with the automatically classified results to calculate errors. The types of error defined in statistical hypothesis testing were used for this study. As shown in Fig. 9, if the blue solid lines represent a manual classification and the dashed lines represent an automatic classification, then the image is separated into four parts: true positive (TP), true negative (TN), false positive (FP), and false negative (FN). If e_I and e_{II} denote Type I and Type II errors, respectively, then Type I error (or FP rate) has the form of

$$e_I = \frac{\text{FP}}{\text{FP} + \text{TN}} 100\%. \quad (36)$$

Type II error (or FN rate) has the form of

$$e_{II} = \frac{\text{FN}}{\text{FN} + \text{TP}} 100\%. \quad (37)$$

Adjusting the value of the threshold can reduce Type I error and increase Type II error or vice versa. An ideal threshold would have that the sum of Type I and Type II errors are minimized. From 0.05 to 5 with steps of 0.05, 100 thresholds were tested using the training data, and when $t_n = 0.45$ the sum of Type I and Type II errors are minimized.

The second method used a spectral angle mapper (SAM) for classification. First, the target spectral signature, which is the sample mean of the spectral signature of leaf insects, was calculated using the same training data described above. The spectral

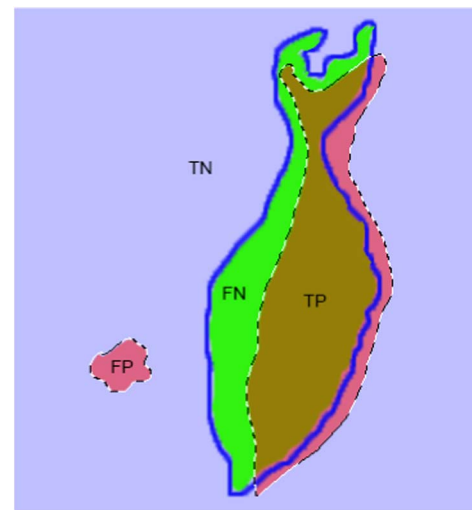


Fig. 9. Definition of errors.

angle between the spectral signature of a pixel to the target can be calculated and is denoted by s in the domain $[0, \pi/2]$. The spectral angle s is normalized to $[0,1]$ using

$$N_s = s/(\pi/2), \quad (38)$$

where N_s is the normalized value of spectral angle s . Figure 8(f) shows an example image of the normalized spectral angle N_s . As in the method using NDVI, an empirical threshold $t_s = 0.45$ was obtained using the training data, and, therefore, the images can be classified.

The third method used hyper-hue for classification. Similar to the second method, the target values of hyper-hue were first obtained from the training data. Then the Euclidean distance between the hyper-hue of a pixel and the target can be calculated and is denoted by d , which is in the domain of $[0,2]$. The distance of hyper-hue d is normalized to $[0,1]$ by

$$N_d = d/2, \quad (39)$$

where N_d is the normalized form of the distance of the hyper-hue. Figure 8(g) is an example image of N_d , and Figs. 8(i)–8(l) show the images of the four dimensions of hyper-hue. Similarly, the threshold $t_d = 0.45$ of d was obtained from the training data, and then the image can be classified.

The remaining 100 sets of images were used for testing the algorithms, and the results of the experiment are listed in Table 2. The method using hyper-hue achieved the least Type I error, 10.8%. Compared with the Type I error of NDVI 22.6% and SAM 16.4%, the advantage of using hyper-hue to

Table 2. Errors of Different Methods for Classification

	NDVI (%)	SAM (%)	DHH ^a (%)
Type I	22.6	16.4	10.8
Type II	10.1	12.6	12.1
Sum of Types I and II	32.7	29.0	22.9

^aDHH indicates the method that uses the distance of hyper-hue.

classify the insects from bush leaves is clear. For Type II error, the three methods have similar results. The method using hyper-hue has a Type II error 12.1%, which is close to that of SAM (12.6%) and NDVI (10.1%). As a final result, the method using hyper-hue achieved the least error in the sum of Type I and Type II errors. From observation of Figs. 8(e), 8(f), and 8(j), the contrast of the image of N_b is better than that of N_n and N_s ; that is, the pixels of the insect have lower intensity and those of the leaf have higher intensity. This indicates that the distance of hyper-hue can provide more distinctive information than SAM or NDVI for the classification of insects and leaves. In comparison, the distance of hyper-hue can reduce Type I errors without introducing significant Type II errors.

C. Experiment Two: Measure Material Similarities Using Remote Sensed Hyperspectral Images

Human observation of hyperspectral images is one of the generally used approaches for analysis and interpretation of hyperspectral data. This experiment shows that hyper-hue can provide a different viewpoint when human observers are

measuring the similarity of materials in hyperspectral images. The data used is airborne visible/infrared imaging spectrometer (AVIRIS) reflectance data, and it is from National Aeronautics and Space Administration (NASA, <http://www.nasa.gov>, data number f970620t01p02_r03_sc02.a). The spectral bands are from 369 to 2500 nm and there are totally 224 bands with 10 nm bandwidth. 163 bands between 400 and 2000 nm, which have higher signal-noise ratios (SNRs), were selected for processing. For visual observation, the spectral bands of 629.19, 537.33, and 428.91 nm were used to create a color image, as shown in Fig. 10(a). A pixel that represents some green plants was selected as a target, which is marked as red stars in Fig. 10, and the spectral signature of it is shown in Fig. 10(b). Two methods were used to measure the spectral similarity between the target pixel and others. One of the methods is normalized spectral angle, which, except the thresholding step, is similar to the second method used in experiment 2, and the result is shown in Fig. 10(c). Another method used the normalized Euclidean distances of hyper-hue, which is same as the third method in experiment 2 except for the step of

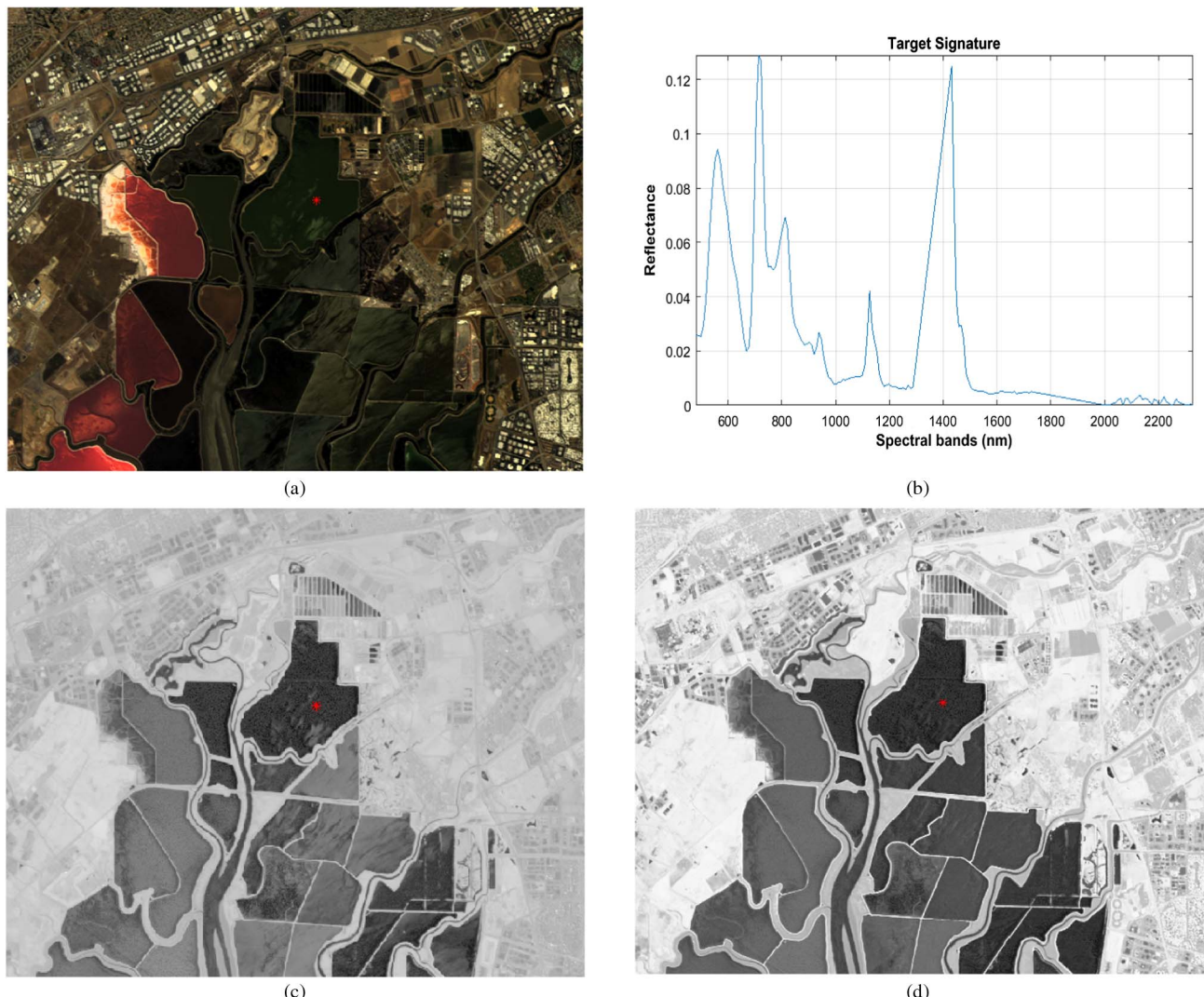


Fig. 10. Measurement of material similarities using SAM and hyper-hue. (a) The color image created of the bands 629.19, 537.33, and 428.91 nm; (b) the target signature; (c) SAM; and (d) distance of hyper-hue.

thresholding, and the result is shown in Fig. 10(d). This experiment was conducted by human observation and the quantitative justice of the result is not provided.

In Figs. 10(c) and 10(d), the darker a pixel, the more similar is the pixel to the target. The results from SAM and the distance of hyper-hue have similar trends in that the pixels of the green plants have lower intensities than those of the soil and buildings. In addition, from observation, the distances of hyper-hue provide different information from SAM, and this additional information would be useful for material classification by observers. For example, in the image of the normalized distance of hyper-hue, the green plants show closer distances to the rivers than that of buildings and roads, but the differences in the image of normalized spectral angle is not clear. The edges in Fig. 10(d) look sharper than those of Fig. 10(c), especially for the buildings.

The algorithms were developed using Matlab 2015b, and the computational speed was tested on a computer with 2.6 GHz CUP and 8G RAM. The size of the hyperspectral images is 500×614 . For the processing of the 163 bands, the average computational time using SAM was 9.3 s. In the new algorithms, the average time used for the transformation from the hypercube to hyper-hue was 18.0 s and that for the calculation of the Euclidean distance of hyper-hue was 1.9 s.

4. CONCLUSION

Formulas were derived that can transform n -dimensional images to a color space called HHSI, which is composed of hyper-hue, saturation, and intensity. The hyper-hue is represented by vectors in $(n - 1)$ dimensions, and it does not introduce loss or distortion of data from dimension reduction. Hyper-hue is independent of saturation and intensity, and, therefore, it is suitable for material classification in a natural environment where illumination is uneven. HHSI space provides an option for analyzing multispectral or hyperspectral images, and it could improve the accuracy of classification for certain types of materials. It should be noted that the selection of classification methods is case by case, and users should choose the best approach based on proper experiments. Only limited experiments are introduced in this paper, and the potential applications of HHSI space should be further investigated.

Funding. Alternate Navigation for Trusted Autonomy (MyIP# 6808).

Acknowledgment. This research was supported by Project Tyche, the trusted autonomy initiative of the Defence Science and Technology Group, Australian Department of Defence.

REFERENCES

1. M. Tkalcic and J. F. Tasic, "Colour spaces: perceptual, historical and applicational background," in *The IEEE Region 8 EUROCON 2003: Computer as a Tool*, Ljubljana, Slovenia, September 24, 2003, pp. 304–308.
2. H. Liu, P. Li, C. Saunders, and S. H. Lee, "Development of a green plant image segmentation method of machine vision system for no-till fallow weed detection," in *Society for Engineering in Agriculture Conference: Innovative Agricultural Technologies for a Sustainable Future* (Engineers Australia, 2013), pp. 95–108.
3. H. Liu, S. H. Lee, and C. Saunders, "Development of a machine vision system for weed detection during both off-season and in-season in broadacre no-till cropping lands," *Am. J. Agric. Biol. Sci.* **9**, 174–193 (2014).
4. V. Cheung, S. Westland, C. Li, J. Hardeberg, and D. Connah, "Characterization of trichromatic color cameras by using a new multispectral imaging technique," *J. Opt. Soc. Am. A* **22**, 1231–1240 (2005).
5. A. R. Smith, "Color gamut transform pairs," *Comput. Graph.* **12**, 12–19 (1978).
6. J. D. Foley and V. Dam, *Fundamentals of Interactive Computer Graphics* (Addison-Wesley, 1982).
7. H. Levkowitz and G. T. Herman, "GLHS: a generalized lightness, hue, and saturation color model," *CVGIP* **55**, 271–285 (1993).
8. R. C. Gonzalez and R. E. Woods, *Digital Image Processing*, 3rd ed. (Addison-Wesley, 1992).
9. F. Perez and C. Koch, "Toward color image segmentation in analog VLSI: algorithm and hardware," *Int. J. Comput. Vis.* **12**, 17–42 (1994).
10. M. D. Fairchild, *Color Appearance Models* (Addison-Wesley, 1997).
11. H. Liu, S. H. Lee, and J. S. Chah, "An evaluation of the contribution of ultraviolet in fused multispectral images for invertebrate detection on green leaves," *Precis. Agric.* **17**, 392–406 (2016).
12. H. Liu and S. Lee, "Stitching of video sequences for weed mapping," in *International Conference on Intelligent Information Hiding and Multimedia Signal Processing (IHIH-MSP)* (IEEE, 2015), pp. 441–444.
13. H. Liu, C. Saunders, and S. H. Lee, "Development of a proximal machine vision system for off-season weed mapping in broadacre no-till fallows," *J. Comput. Sci.* **9**, 1803–1821 (2013).
14. N. P. Jacobson and M. R. Gupta, "Design goals and solutions for display of hyperspectral images," in *IEEE International Conference on Image Processing* (IEEE, 2005).
15. J. S. Tyo and A. Konsolakis, "Principal-components-based display strategy for spectral imagery," *IEEE Trans. Geosci. Remote Sens.* **41**, 708–718 (2003).
16. P. J. Ready and P. A. Wintz, "Information extraction, SNR improvement, and data compression in multispectral imagery," *IEEE Trans. Commun.* **21**, 1123–1131 (1973).
17. G. Buchsbaum and A. Gottschalk, "Trichromacy, opponent colours coding and optimum colour information transmission in the retina," *Proc. R. Soc. London* **220**, 89–113 (1983).
18. S. Prasad and L. Bruce, "Limitations of principal components analysis for hyperspectral target recognition," *IEEE Geosci. Remote Sens. Lett.* **5**, 625–629 (2008).
19. T. Rey, A. Kordon, and C. Wells, *Applied Data Mining for Forecasting Using SAS(R)* (SAS Institute, 2012).
20. S. Karamizadeh, S. M. Abdullah, A. A. Manaf, M. Zamani, and A. Hooman, "An overview of principal component analysis," *J. Signal Inf. Process.* **4**, 173–175 (2013).
21. A. Restrepo, "Tetrachromatic colour space," *Proc. SPIE* **8295**, 82950G (2012).
22. F. A. Kruse, A. B. Lefkoff, J. W. Boardman, K. B. Heidebrecht, A. T. Shapiro, P. J. Barloon, and A. F. H. Goetz, "The spectral image processing system (SIPS)—interactive visualization and analysis of imaging spectrometer data," *Remote Sens. Environ.* **44**, 145–163 (1993).
23. G. P. Petropoulos, K. P. Vadrevu, G. Xanthopoulos, G. Karantounias, and M. Scholze, "A comparison of spectral angle mapper and artificial neural network classifiers combined with Landsat TM imagery analysis for obtaining burnt area mapping," *Sensors* **10**, 1967–1985 (2010).
24. A. Hanbury, "Constructing cylindrical coordinate colour spaces," *Pattern Recogn. Lett.* **29**, 494–500 (2008).
25. D. Arthur and S. Vassilvitskii, "K-means++: the advantages of careful seeding," in *The 18th Annual ACM-SIAM Symposium on Discrete Algorithms* (Society for Industrial and Applied Mathematics, 2007), pp. 1027–1035.
26. H. Liu, S. H. Lee, and J. S. Chah, "A review of recent sensing technologies to detect invertebrates on crops," *Precis. Agric.* **17**, 392–406 (2016).
27. J. W. Rouse, R. H. Haas, J. A. Scheel, and D. W. Deering, "Monitoring vegetation systems in the Great Plains with ERTS," in *Third Earth Resources Technology Satellite Symposium* (NASA, 1974), pp. 309–317.